



# Semi-solid alkali metal electrodes enabling high critical current densities in solid electrolyte batteries

Richard J.-Y. Park<sup>1</sup>, Christopher M. Eschler<sup>1</sup>, Cole D. Fincher<sup>1,2</sup>, Andres F. Badel<sup>1</sup>, Pinwen Guan<sup>3</sup>, Matt Pharr<sup>2</sup>, Brian W. Sheldon<sup>4</sup>, W. Craig Carter<sup>1</sup>, Venkatasubramanian Viswanathan<sup>3</sup> and Yet-Ming Chiang<sup>1</sup>✉

**The need for higher energy-density rechargeable batteries has generated interest in alkali metal electrodes paired with solid electrolytes. However, metal penetration and electrolyte fracture at low current densities have emerged as fundamental barriers. Here we show that for pure metals in the Li–Na–K system, the critical current densities scale inversely to mechanical deformation resistance. Furthermore, we demonstrate two electrode architectures in which the presence of a liquid phase enables high current densities while it preserves the shape retention and packaging advantages of solid electrodes. First, biphasic Na–K alloys show K<sup>+</sup> critical current densities (with the K-β''-Al<sub>2</sub>O<sub>3</sub> electrolyte) that exceed 15 mA cm<sup>-2</sup>. Second, introducing a wetting interfacial film of Na–K liquid between Li metal and Li<sub>6.75</sub>La<sub>3</sub>Zr<sub>1.75</sub>Ta<sub>0.25</sub>O<sub>12</sub> solid electrolyte doubles the critical current density and permits cycling at areal capacities that exceed 3.5 mAh cm<sup>-2</sup>. These design approaches hold promise for overcoming electrochemomechanical stability issues that have heretofore limited the performance of solid-state metal batteries.**

Rechargeable batteries have enabled advances in portable electronics, transportation and renewable energy storage over the past two decades. Today's electric vehicle lithium (Li)-ion batteries possess a combination of a high specific energy (~150 Wh kg<sup>-1</sup> at pack-level) and a high energy density (~250 Wh l<sup>-1</sup> at pack level)<sup>1</sup> with a cycle life that is on track to reach 5,000 cycles<sup>2</sup>. However, future applications, such as electric aviation<sup>3</sup>, will require additional radical improvements. One promising approach is to use metallic negative electrodes, especially Li (ref. 4), which provides for a high cell voltage and capacity (3,869 mAh g<sup>-1</sup> and 2,066 Ah l<sup>-1</sup> theoretical capacities).

However, the use of Li metal anodes with liquid electrolytes has met serious challenges, most importantly a poor coulombic efficiency and susceptibility to short circuits due to dendrite formation at practical current densities (1–3 mA cm<sup>-2</sup>) (refs. 5,6). An alternative approach pairs Li metal anodes with inorganic solid electrolytes, and could result in safer as well as energy-dense batteries<sup>4,7–9</sup>. Inorganic solid electrolytes, such as Li sulfides (for example, β-Li<sub>3</sub>PS<sub>4</sub>) and garnet-structure oxides (for example, Li<sub>7</sub>La<sub>3</sub>Zr<sub>2</sub>O<sub>12</sub>), have received much attention due to their high ionic conductivity<sup>10,11</sup> and progress towards achieving an electrochemically stable electrode–electrolyte interface<sup>8</sup>. However, despite expectations that the high elastic moduli of inorganic solid electrolytes (~20 GPa for sulfides<sup>12</sup> and ~100–200 GPa for oxides<sup>13</sup>) compared with that of Li metal (~5 GPa) would suppress Li dendrites<sup>14</sup>, a hallmark of both single crystalline<sup>15,16</sup> and polycrystalline<sup>15,17–21</sup> Li solid electrolytes is penetration by metal filaments on deposition at a critical current density (CCD) in the range 0.1–1 mA cm<sup>-2</sup> (at room temperature), too low for most practical applications. Recent experiments with sodium (Na) metal electrodes showed higher room-temperature deposition CCDs of 3.0 mA cm<sup>-2</sup> at an areal capacity of ~0.5 mAh cm<sup>-2</sup> (with a relatively high applied pressure of 4–12 MPa) (ref. 22) and as high as

12 mA cm<sup>-2</sup> at an areal capacity of 0.25 mAh cm<sup>-2</sup> (applied pressure of 3.4 MPa) (ref. 23).

Here we demonstrate a semi-solid (that is, multiphase liquid–solid) electrode approach that takes advantage of the high CCD of liquid metal electrodes, but with the shape retention and cell packaging advantages of solid metal electrodes. We first show that the pure alkali metals, Li, Na and potassium (K), when mated with solid electrolytes that conduct each respective alkali ion, have CCDs that scale inversely to their mechanical deformation resistance. We then demonstrate that biphasic Na–K alloys, paired with a K-β''-Al<sub>2</sub>O<sub>3</sub> (KBA) solid electrolyte, can be cycled between liquid-rich and solid-rich end states at CCDs several times higher than those achievable with the solid-state alkali metals. Furthermore, the high areal capacities at which such behaviour is realized suggests 'self-healing' of electrodeposition-induced defects at the metal–solid electrolyte interface. Na–K alloys permit cycling at a CCD that exceeds 15 mA cm<sup>-2</sup>, the highest room-temperature value reported to date for a metal electrode on a solid electrolyte, and sufficient to enable 3C cycling at a typical Li-ion electrode area capacity (that is, 3 mAh cm<sup>-2</sup>). Finally, by introducing a small amount of Na–K liquid at the interface between a Li metal electrode and Li<sub>6.75</sub>La<sub>3</sub>Zr<sub>1.75</sub>Ta<sub>0.25</sub>O<sub>12</sub> (LLZTO) solid electrolyte, we show that the CCD more than doubles with cycling at practical areal capacities >3 mAh cm<sup>-2</sup>, which suggests that degradation by void formation in solid metal electrodes<sup>24</sup> can be mitigated with a thin metallic liquid film.

## Critical phenomena leading to metal filament penetration

The threshold conditions for the extension of a metal filament through a solid electrolyte can be described in terms of either a critical overpotential or current density. Conceptually, both are correlated with the presence of flaws in the solid electrolyte, which are

<sup>1</sup>Department of Materials Science & Engineering, Massachusetts Institute of Technology, Cambridge, MA, USA. <sup>2</sup>Department of Mechanical Engineering, Texas A&M University, College Station, TX, USA. <sup>3</sup>Department of Mechanical Engineering, Carnegie Mellon University, Pittsburgh, PA, USA. <sup>4</sup>School of Engineering, Brown University, Providence, RI, USA. ✉e-mail: [ychiang@mit.edu](mailto:ychiang@mit.edu)

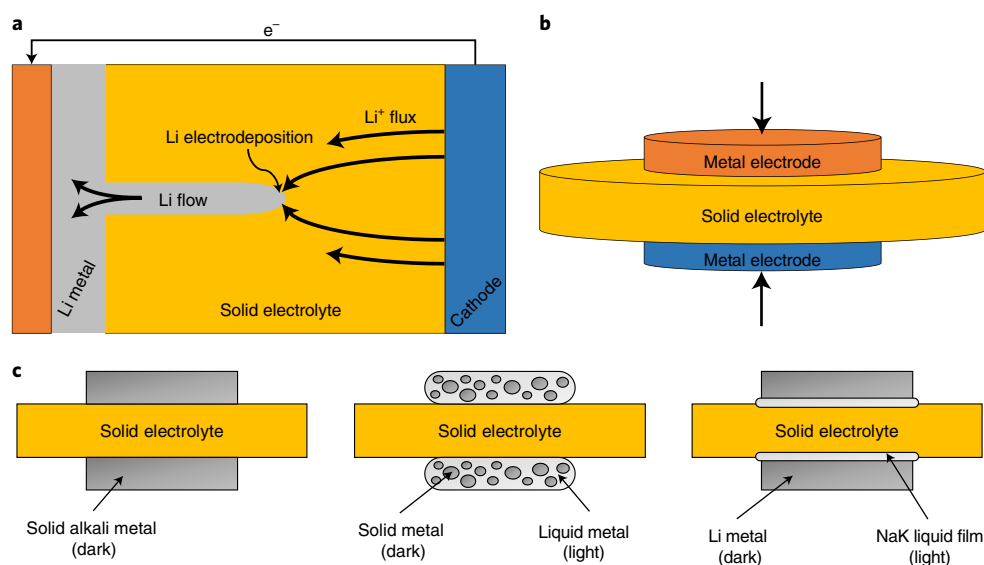


**Fig. 1 | Overview of the electrochemical cells studied.** **a**, Li flux through a solid electrolyte results in electrodeposition at the tip of metal-filled flaws, which readily exceed the critical overpotential for fracture<sup>15</sup> unless there is metal flow to relieve the stress. CCD is reached when electrodeposition rate exceeds the metal flow rate. **b**, Schematic of symmetric cell configuration for CCD measurements. **c**, Graphical schematic summarizing the three families (all-solid, semi-solid and solid with an interfacial liquid) of electrode materials investigated in this study.

filled with electrodeposited metal when the applied potential produces a flux of metal ions through the solid electrolyte (Fig. 1a). As elaborated by Porz et al.<sup>15</sup>, metal-filled defects will propagate through solid electrolytes as a result of crack-opening stresses generated by the electrodeposition of metal that are high enough to fracture the electrolyte. Li accumulation inside a flaw has an associated increase in volume that produces tensile loading of the flaw, which results in crack propagation when the elastic energy release rate exceeds the fracture resistance of the electrolyte<sup>15</sup>. The electrical overpotential that produces this stress is the critical overpotential, and represents a thermodynamic limit dependant on properties such as the solid electrolyte fracture toughness<sup>12,15,16</sup> and the surface flaw size distribution. As in the Griffith–Inglis–Orowan theory of fracture<sup>25–27</sup>, the largest such flaw in the solid electrolyte will have the lowest critical overpotential and tend to propagate first.

However, material transport away from regions of high stress such as the metal filament tip, can relieve the electrodeposition stresses; this is fundamentally the origin of the CCD. As the current density is equivalent to the atomic electrodeposition rate (assuming a 100% Coulombic efficiency), at low enough deposition rates a ductile electrodeposited metal may flow away from electrodeposition sites rapidly enough to allow the crack-tip stresses to remain subcritical. The CCD therefore corresponds to an electrodeposition rate that exceeds the metal flow rate necessary to maintain a subcritical stress. Prior work with liquid Na electrodes in high-temperature sodium–sulfur batteries considered analogous mechanical models, using Poiseuille flow of the liquid metal to relate the stress at the Na-filled crack to the rate of metal extrusion out of the crack set by the applied current density<sup>28,29</sup>. For solid metals, ‘extrusion’ from the metal-filled crack requires creep and plastic deformation. At high homologous temperatures, creep imparts an effective viscosity and so the solid metals may behave as an ‘incompressible work fluid’. For Li metal, the bulk deformation behaviour was recently characterized in detail<sup>30,31</sup>, although size effects may also come into play at the submicrometre length scales that may be most relevant in typical solid electrolytes<sup>30,32</sup>.

In this work, symmetric electrochemical cells of the configuration in Fig. 1b were used to measure the CCD at room temperature

in a total of 38 cells with six distinct combinations of metal electrodes and solid electrolytes, tabulated in Supplementary Table 1. The cells fall within three categories, as depicted in Fig. 1c: first, solid Li, Na and K electrodes paired with their respective ion-conducting solid electrolytes, second, semi-solid Na–K electrodes paired with a K ion conducting solid electrolyte and, third, a Li metal solid electrolyte with a thin interfacial film of Na–K liquid, paired with the LLZTO solid electrolyte.

### CCDs for Li, Na and K metal electrodes

The pure alkali metals Li, Na and K were electrodeposited, respectively, through the solid electrolytes LLZTO, Na- $\beta''$ -Al<sub>2</sub>O<sub>3</sub> (NBA) and KBA. The three metals in their solid state differ markedly in their mechanical properties, decreasing by over a factor of three in shear modulus (at 300 K) and yield stress (at 80 K) in the order Li  $\rightarrow$  Na  $\rightarrow$  K (refs. 33,34) (Supplementary Table 2). Their liquid-state viscosities when melted also increase in this order<sup>35,36</sup>. Moreover, Na metal possesses a substantially lower yield stress and increased susceptibility to creep than did Li metal at bulk and on small scales<sup>30,37</sup>. We furthermore conducted microhardness testing experiments on Li, Na and K metals to directly measure the metal’s resistance to flow. The equivalent yield stress, which is taken as one-third the hardness for ductile metals<sup>38</sup>, decreased in the order Li (1.74 MPa) to Na (0.41 MPa) to K (0.24 MPa) (Fig. 6b). We expect a softer metal to exhibit a higher CCD under equivalent conditions (for example, stack pressure).

However, the properties of the solid electrolytes also affect the CCD. We sought a set of solid electrolytes that would allow a direct comparison of behaviour between the three pure metal electrodes across all three working ions (Li<sup>+</sup>, Na<sup>+</sup> and K<sup>+</sup>). The three solid electrolytes used, LLZTO, NBA and KBA, were each obtained as densely sintered polycrystalline discs (Fig. 2a,b) and determined by X-ray diffraction to be predominantly composed of the desired ion-conducting crystalline phase (Supplementary Table 3). As described in the Methods, these solid electrolytes can be processed to a similar smooth surface finish (Supplementary Fig. 1) and possess similar fracture toughness (2–3 MPa m<sup>0.5</sup>; Supplementary Fig. 2) and ionic conductivities (1–2 mS cm<sup>-1</sup>; Supplementary Fig. 3). For each combination of metal electrode and solid electrolyte, the CCD

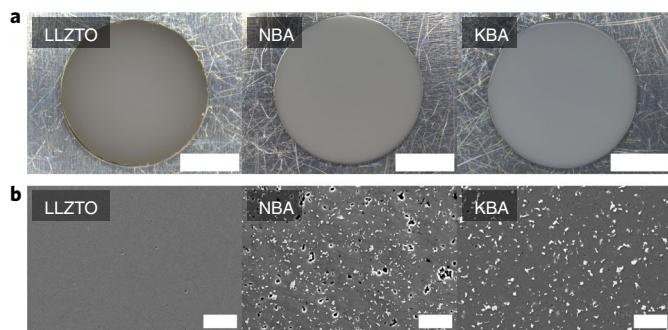


**Fig. 2 | Surface finish and microstructure of solid electrolytes studied. a,b,** Polished discs (**a**) and secondary electron images (**b**) of (left to right)  $\text{Li}^+$ -,  $\text{Na}^+$ - and  $\text{K}^+$ -conducting solid electrolytes. Scale bars, 5 mm (**a**); 20  $\mu\text{m}$  (**b**).

was measured in a symmetric cell by reversibly plating the metal in both directions at stepwise increasing galvanostatic currents until the current and potential drop across the cell indicated the onset of a short circuit (Fig. 3a). Impedance spectroscopy was then used to confirm the short circuit (Fig. 3b). After cycling to failure, each cell was disassembled for examination. A representative example of data for each metal electrode type appears in Fig. 4a–c and Supplementary Figs. 4–9. The features visible in these post-mortem images, alongside the specific details of the polarization curves are discussed in Supplementary Discussion.

The room-temperature CCDs for Na metal and K metal are clearly higher than that for Li metal, as both reach maximum values of  $\sim 3 \text{ mA cm}^{-2}$  versus  $< 1 \text{ mA cm}^{-2}$  for Li (Figs. 5a and 6a). Each datum in Fig. 5a,b represents one cell from these experiments as listed in Supplementary Table 1. The vertical lines at  $1 \text{ mAh cm}^{-2}$  and  $3 \text{ mAh cm}^{-2}$  in Fig. 5 represent, respectively, a minimum areal capacity for practical application, and a typical areal capacity for current Li-ion technology. The horizontal lines at  $1 \text{ mA cm}^{-2}$  and  $3 \text{ mA cm}^{-2}$  in Fig. 5 represent CCD values that correspond to a 1C rate capability at those areal capacities. We focused on areal capacities in the range  $1\text{--}4 \text{ mAh cm}^{-2}$  because results at a lower areal capacity may not be relevant to high energy density batteries. For example, a high cycling stability has been observed in solid-state

thin-film batteries<sup>39</sup>, in which areal capacities are over a factor of five lower than those in bulk batteries. Recent studies for Na metal in contact with NBA reported higher CCDs than we measured here, but at lower areal capacities:  $3 \text{ mA cm}^{-2}$  at  $0.5 \text{ mAh cm}^{-2}$  (ref. 22) and  $12 \text{ mA cm}^{-2}$  at  $0.25 \text{ mAh cm}^{-2}$  areal capacities<sup>23</sup>. We are not aware of prior results for K metal. The areal capacities employed here are also several times higher than those in prior work using bulk Li metal foil electrodes, as shown by the results in Li/LLZTO/Li cells (Fig. 5a,b and on an expanded scale in Supplementary Fig. 10). The highest areal capacities we tested for Li metal ( $\sim 3.8 \text{ mAh cm}^{-2}$ ) are nearly ten times higher than those at the high end of the range available in the literature.

Note that results in Fig. 5a,b show a variation in areal capacity even between nominally identical experiments. This is because both the CCD and areal capacity shown are true values based on the final measured area of the metal electrodes in the disassembled cell, which exhibits some variability, rather than on the areas of the current collectors or starting electrodes.

We also expect a distribution of CCDs to be observed in these experiments, in large part because the short-circuit event is correlated with the failure of a brittle solid. It is widely accepted that brittle materials exhibit a wide distribution of measured strengths (which is normally treated with Weibull statistics) due to the existence of the distribution of defect types and sizes. Fracture is inherently stochastic as it is the largest flaw in the distribution to cause failure. Similarly, it is not surprising that measured CCD values should exhibit a range of values if failure propagates from defects and inhomogeneities at the metal–solid electrolyte interface, or even below the surface. Note that the electrode area ( $\sim 1 \text{ cm}^2$ ) is many orders of magnitude larger than the scale of the microstructure (tens of square micrometres; Fig. 2b), which ensures that a range of flaws will be tested. We nonetheless observed a higher average CCD as well as a higher peak CCD for the Na and K metals compared to the Li metal. The microstructure and porosity distribution of the three solid electrolytes used here are described in the Supplementary Discussion.

Having measured the CCD as well as the equivalent yield stress of each metal from microhardness experiments, we are able to show that, within the error limits of the data, there is an approximately linear relationship between the two (Fig. 6b). Note that this trend is observed across solid electrolytes of nearly identical ionic

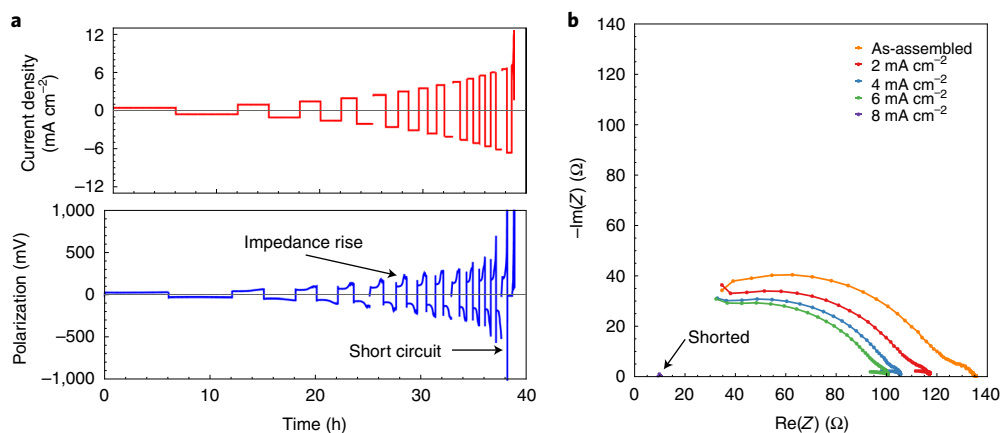


**Fig. 3 | CCD for the metal penetration of solid electrolytes. a,** Typical current density versus time sequence (top) and corresponding potential profile (bottom), here for a K/KBA/K symmetric cell reversibly plating  $3 \text{ mAh cm}^{-2}$  of K metal. The onset of cell failure, which serves as the measurement of the CCD, is indicated by the arrow. The impedance rise is discussed in later sections of the article. The onset of an electrical short circuit is detected as a voltage drop across the cell. **b,** Nyquist plot for the same cell. The curves that connect the individual data points act as guides for the eye. The curves correspond to the impedance spectra taken after cycling the cell at the particular current density shown in the key. The presence of the capacitive arcs indicates the absence of a short circuit. A short circuit is confirmed by the collapse of the spectrum to a point, as indicated by the arrow.

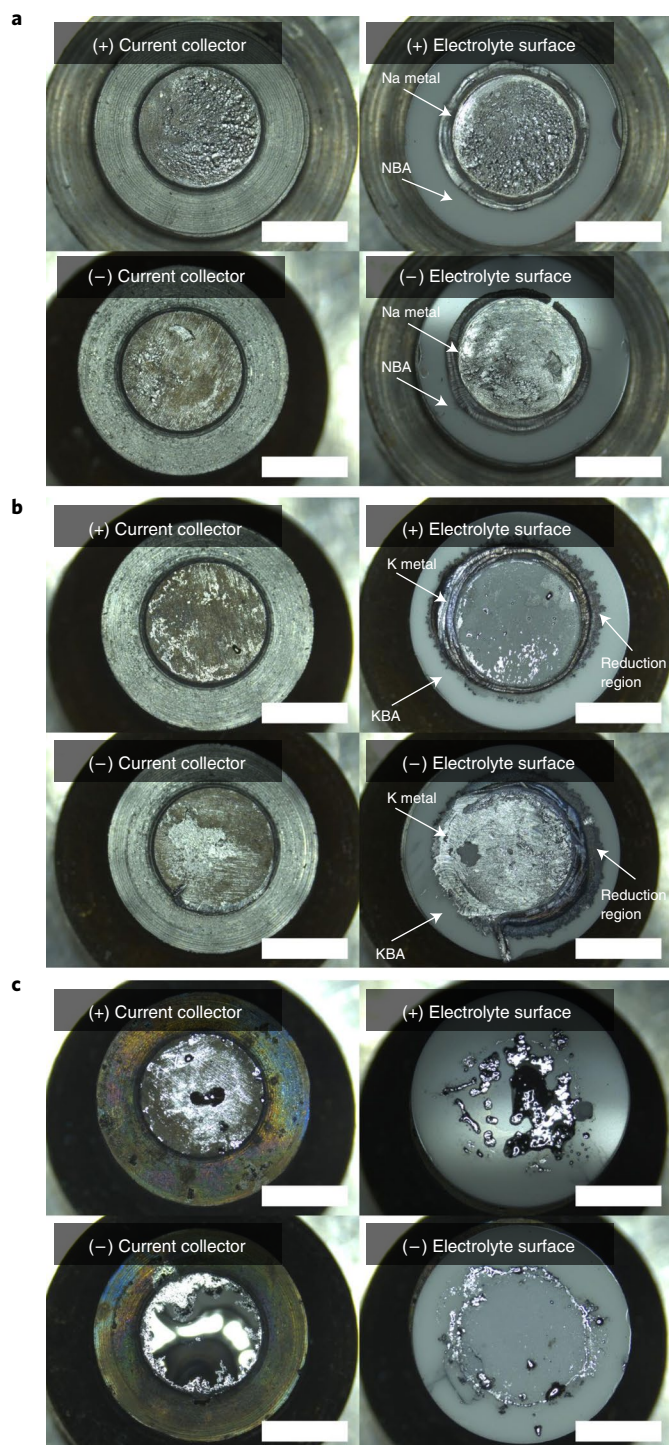


**Fig. 4 | Surfaces of positive and negative current collectors and solid electrolyte after cycling of the symmetric metal–solid electrolyte cells to short-circuit failure. a**, Na metal electrodes. **b**, K metal electrodes. **c**, 0.95K–0.05Na (by mole) semi-solid electrode. The arrows point to the probable location of the metal-filled crack(s) that cause the short circuit. Scale bars, 5 mm.

conductivity ( $\sim 1 \text{ mS cm}^{-1}$ ) and fracture toughness ( $\sim 2\text{--}3 \text{ MPa m}^{0.5}$ ), and in experiments at a similar plated areal capacity ( $1.5\text{--}3 \text{ mAh cm}^{-2}$ ). This result is consistent with the flow-based model discussed above, in which the CCD is limited by the Poiseuille flow of the metal out of stress-concentrating flaws. These results for the three

solid metals also establish a baseline behaviour for comparison with the results for semi-solid alloy electrodes, reported below.

### Semi-solid electrodes increase CCD

Several recent studies focused on use of room-temperature liquid metal electrodes, obtained from deep eutectics in Na–K (ref. <sup>40</sup>), Na–Cs (ref. <sup>41</sup>) and Ga–In (ref. <sup>42</sup>). A limitation of fully liquid electrodes is that the corresponding electrochemical cells must be designed around containment of the low-viscosity liquid metal, as in the case of high-temperature sodium–sulfur batteries, in which closed-ended ceramic electrolyte tubes are typically used. Such designs may be costly or impractical, especially for compact high-energy battery packs in which a large number of series-connected cells are needed to reach the design voltage. Our approach, instead, aims to use semi-solid mixtures which, include a liquid phase in which the working alkali metal is soluble. The liquid phase provides a fast transport path for the working ion as well as flow at the microscale, which enables a high CCD, whereas the solid phase provides structural rigidity and is a source of the working ion. In the following examples, the semi-solid electrodes have the consistency of a paste and can be assembled into a free-standing cell without specialized liquid-electrode containment.

In Fig. 7a, composition A has a starting composition of 0.95K–0.05Na (by mole) and becomes enriched in K on charging in a K-ion cell design in which the cathode supplies the working  $\text{K}^+$  and is assembled in the discharged state. Cycling to an areal capacity of  $3 \text{ mAh cm}^{-2}$  (which corresponds to an electrode thickness change of  $\sim 51.5 \mu\text{m}$ ) causes a composition swing in the Na–K electrode, as indicated by the left-pointing blue arrow in Fig. 7a. At the end of the half-cycle, the Na–K electrode composition terminates as a mixture that is mostly the K-rich solid phase  $\alpha$ , mixed with a small amount of liquid (3.8 mol%). (This is for the starting electrode of  $\sim 10 \mu\text{l}$  total volume and  $\sim 150 \mu\text{m}$  thickness (Methods).) Composition B has a higher Na starting composition of 0.90K–0.10Na (by mole) and behaves similarly, except that it has a higher liquid fraction throughout, which terminates the half-cycle (left-pointing red arrow) with the same two phases, but ten times as much Na–K liquid (38 mol%). Additional details of the electrode depletion and enrichment during cell cycling are available in the Supplementary Discussion. Cells that used compositions A and B reached maximum CCDs as high as  $8 \text{ mA cm}^{-2}$  and  $20 \text{ mA cm}^{-2}$ , respectively. The average CCD values (based on  $N=4$  and  $N=3$  cells, respectively) are  $\sim 4$  times and  $\sim 6$  times higher than that achieved with K metal alone (Fig. 5b and Fig. 6a). The CCDs reached with composition B (mean value of  $14 \text{ mA cm}^{-2}$  at areal capacities of  $1.5\text{--}2 \text{ mAh cm}^{-2}$ ) also exceeded the highest reported room-temperature value for solid Na metal cells ( $12 \text{ mA cm}^{-2}$ , measured at a much lower areal capacity of  $0.25 \text{ mAh cm}^{-2}$ ) (ref. <sup>23</sup>). The results demonstrate that even a small percentage of co-existing liquid is effective in increasing the CCD of an alkali metal electrode. Examination of Supplementary Figs. 7 and 8, respectively, indicates that the area specific resistance of the 0.95K–0.05Na/KBA/0.95K–0.05Na cell and the 0.90K–0.10Na/KBA/0.90K–0.10Na cell are both on the order of  $\sim 30 \Omega \text{ cm}^2$ ; the difference in CCD is not correlated with any meaningful difference in interfacial area specific resistance.

### Interfacial liquid film increases CCD

Given that Li-ion technology is more well-developed than Na-ion or K-ion technologies, we also considered semi-solid anode design possibilities in which Li is the working ion. In the Li–Na and Li–K binary systems, the equilibrium liquid fields do not extend all the way to room temperature (see phase diagrams in Supplementary Fig. 11), so room-temperature semi-solid electrodes are not available. In contrast, the Na–K eutectic at 260.5 K (Fig. 7a) indicates at least a limiting composition (0.32Na–0.68K, by mole) in which a room-temperature liquid can be accessed. Thus, an electrode

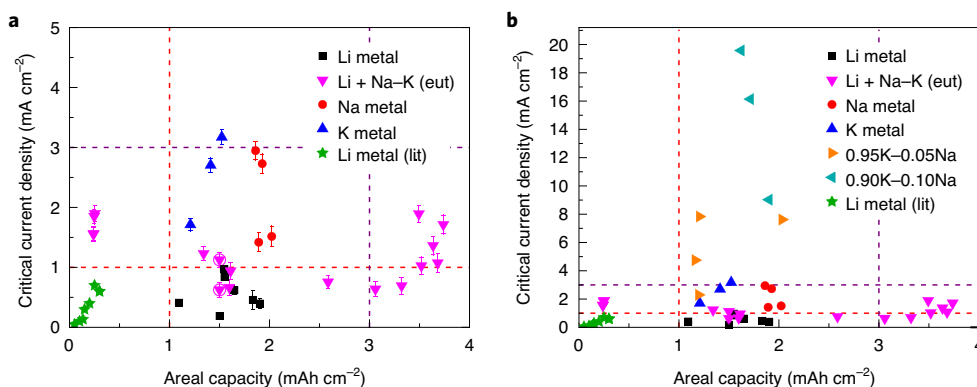


**Fig. 5 | CCD versus areal capacity for single-phase solid metals and semi-solid alloy mixtures.** **a**, CCDs for single-phase solid Li, Na and K metal in symmetric cells using the solid electrolytes LLZTO, NBA and KBA, and a 0.68K–0.32Na (by mole) eutectic liquid (eut) at the interface between Li metal foil and LLZTO. All the experiments were conducted at 20 °C under a nominal stack pressure of  $-1.5$  MPa, except for circled points, which are from experiments conducted at  $-75$  kPa. **b**, CCDs for all the metal electrodes measured, which include 0.95K–0.05Na (by mole) and 0.90K–0.10Na (by mole) semi-solid alloys. Each datum represents an independent cell measurement. The total span of the error bars in **a** represents the variation in CCD for a single increment by which the current density was stepped in the galvanostatic protocol. The respective error bars in **b** are not visible as the marker size exceeds the span of the bars in the given axis scale. Lit refers to comparable data points for Li metal in the literature (Supplementary Fig. 10).

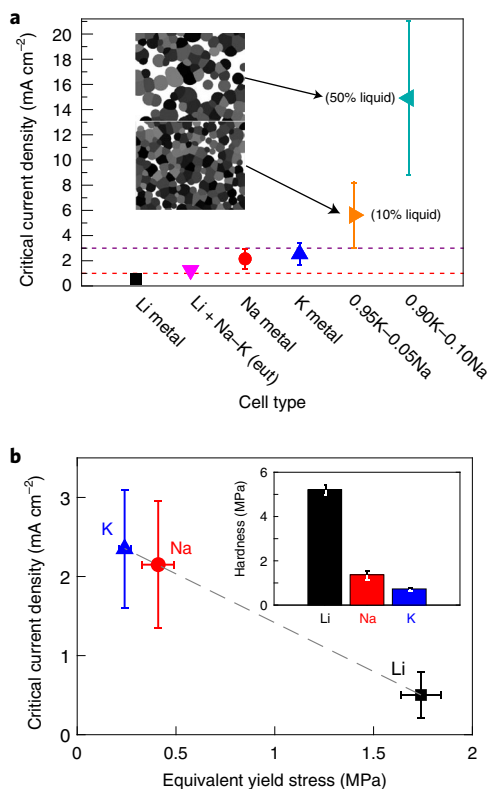


**Fig. 6 | CCD versus electrochemical cell type and alkali metal yield stress.**

**a**, Average CCD value for each metal or alloy, which includes results across all areal capacities tested. Inset: a simulation (Methods) of the expected electrode microstructures for the semi-solid experiments, in which the liquid phase appears as white and the solid crystalline phase particles as shades of grey. **b**, CCD versus equivalent yield stress (defined as hardness/3 (ref. <sup>38</sup>)) for solid Li, Na and K metal in this study. The grey line serves as a guide for the eye. Inset: hardness for bulk Li, Na and K metal. Each bar represents the average of ten tests, and the error bar represents the standard deviation. These results indicate that the equivalent yield stress decreases in the order Li ( $1.74 \pm 0.1$  MPa) to Na ( $0.41 \pm 0.08$  MPa) to K ( $0.24 \pm 0.03$  MPa). The vertical error bars represent 95% confidence intervals for the CCD according to the sample set. The horizontal error bars in **b** represent the standard deviation of the measured values.

design in which a thin Na–K liquid film is used in conjunction with a solid Li metal electrode was conceived (Fig. 1c, right panel). The Li–Na–K ternary phase diagram (Fig. 7b) was calculated to determine the co-existing phases and compositions present in such an electrode. The isothermal section of this ternary diagram at 300 K shows a wide two-phase field (the triangle with blue lines) within which solid Li (the body-centred cubic (BCC) phase) co-exists with the Na–K liquid in a simple two-phase equilibrium. The blue lines are tie lines that join the co-existing solid and liquid compositions and show that the solid Li metal phase co-exists with liquid alloy that can take on a wide range of Na/K ratios. The Na–K liquid dissolves a small amount of Li, a solubility that cannot be resolved in Fig. 7b. The solubility was also calculated and is shown in Fig. 7c. The solubility of Li is highest in Na-rich liquids and decreases by about a factor of 20 from the Na-rich to K-rich liquids that can co-exist with Li metal, but the Li solubility in the liquid is less than 1% throughout. There are no ternary phases.

Based on this understanding, we constructed cells in which a thin layer of the Na–K eutectic liquid was placed at the interface between LLZTO and a Li metal foil electrode. This interfacial metal film may serve one or both of two functions. The first is to transport Li from the solid Li metal electrode to the solid electrolyte while maintaining a conformal liquid layer of negligible yield stress, and thereby raise the CCD. The second is to act as an electronically conductive ‘liquid current collector’ that can flow to fill any voids that would otherwise form in the solid Li electrode during stripping and plating. In this role, the liquid metal film may homogenize the plating current density, which reduces the risk for short circuits and enables higher areal capacities. One or both functions provide ‘self-healing’ characteristics to the electrode as they mitigate the formation of interfacial defects that are exacerbated on cycling.

We performed sessile-drop wetting experiments, which showed that the Na–K eutectic alloy has a lower contact angle on LLZTO than that of any of the pure alkali metals (Supplementary Fig. 12) at temperatures at which all are liquid, and lower than that of the contact angle of solid Li on LLZTO<sup>43</sup>. This indicates that in our cell design, the Na–K eutectic liquid will wet the LLZTO in preference to the solid Li metal, and thereby remain as an interfacial film between the LLZTO and Li metal.

Cycling tests were conducted over a wide range of areal capacities from 0.25 to 3.7 mAh cm<sup>-2</sup> (Fig. 5a,b). Compared with the control cells using Li metal alone, both the average and the maximum CCD values are higher by about a factor of two. The average CCD

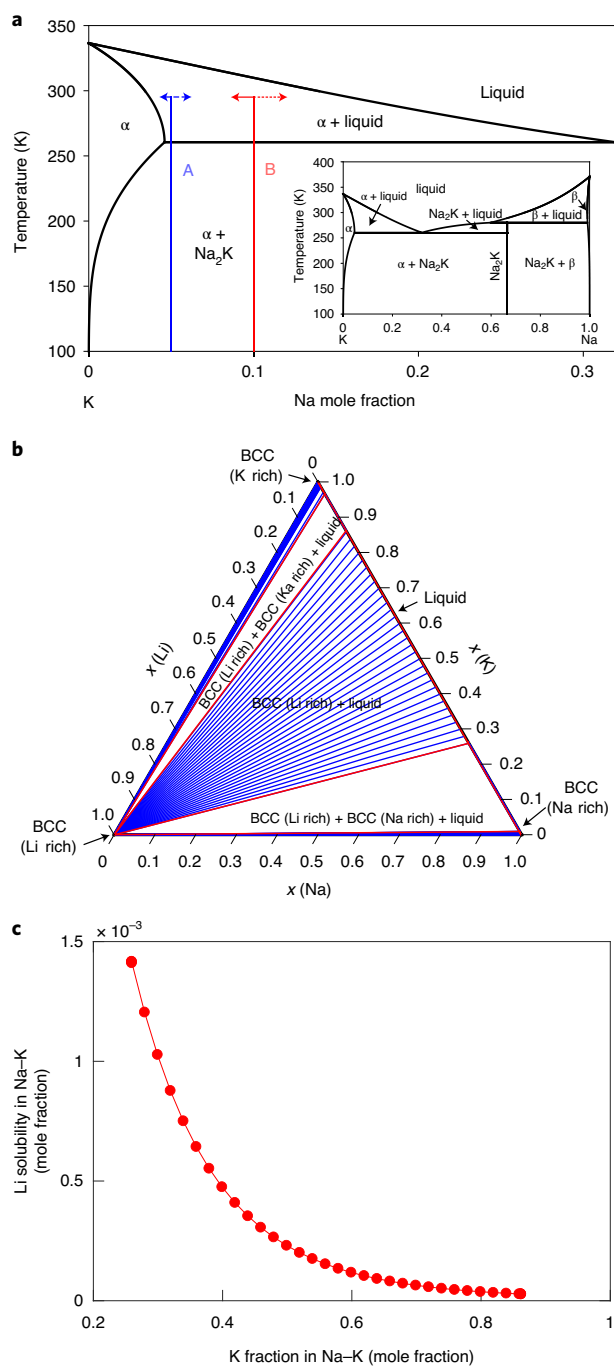


**Fig. 7 | Compositional design for semi-solid alkali metal electrodes.**

**a**, K-rich end of the computed Na-K binary phase diagram. Inset: full phase diagram. Compositions A (0.95K-0.05Na) and B (0.90K-0.10Na) are shown by the vertical blue and red lines, respectively. The horizontal arrows that point to the left and right show the composition change in each electrode of this symmetric cell design on cycling to a  $3 \text{ mAh cm}^{-2}$  areal capacity. For composition A, the calculated initial and terminal liquid phase percentages in the two electrodes of the symmetric cell are 3.8 mol% and 20 mol%, respectively, whereas for composition B they are 38 mol% and 70 mol%, respectively. **b**, Isothermal section of Li-Na-K at 300 K. The high mixing enthalpy between BCC Li and Na/K liquid leads to a low solubility of each in the other. A wide two-phase field exists within which nearly pure BCC Li co-exists with the Na-K liquid (tie lines shown in blue). **c**, The solubility of Li in the Na-K liquid decreases sharply with an increasing K concentration of the liquid. The solid red curve serves as a guide for the eye.

increased from  $0.50 \text{ mA cm}^{-2}$  (Li) to  $1.21 \text{ mA cm}^{-2}$  (Li-NaK), and for the latter several cells approached  $2 \text{ mA cm}^{-2}$  (Fig. 5a). Equally important, however, the higher CCDs with the alloy approach could be accessed at areal capacities as high as  $3.8 \text{ mAh cm}^{-2}$ , which is nearly an order of magnitude higher than the highest values in previous literature studies for Li metal, in which areal capacities are  $< 0.40 \text{ mAh cm}^{-2}$  (Fig. 5 and Supplementary Fig. 10). The low and stable impedance of the cells using the Na-K liquid throughout the cycling experiments suggests a low chemical reactivity between the Na-K liquid and LLZTO. In our wetting experiments, there also was no evidence of reactivity between the Na-K liquid and polished LLZTO surfaces.

From these results we infer, first, that Li is transported through the Na-K liquid layer and, second, that a thin continuous film of the Na-K liquid is retained at the LLZTO-Li metal interface. When the Li metal is removed from the solid electrolyte surface, the Na-K liquid, which is distinguishable from the Li metal by its high reflectivity, remains on both the LLZTO surface and the Li metal disc. The thickness and volumetric distribution of the interfacial Na-K layer during cell cycling are discussed in the Supplementary Discussion.

In addition, features were observed in the electrochemical tests that support the interpretation that interfacial defects, such as voids formed during Li stripping, are indeed 'healed' in the presence of interfacial Na-K liquid. For the cells with purely Li metal electrodes, attempts to cycle them to current densities greater than  $\sim 1 \text{ mA cm}^{-2}$  were unsuccessful due to an 'open-circuit' failure mode characterized by a large impedance rise after several galvanostatic cycles. An example of such an impedance rise is seen in Supplementary Fig. 4a, and starts at the fourth cycle of the Li/LLZTO/Li symmetric cell cycling at a  $0.5 \text{ mA cm}^{-2}$  current density with a  $1.5 \text{ mAh cm}^{-2}$  areal capacity ( $\sim 7.5 \mu\text{m}$  Li metal deposited per half-cycle) and continues in subsequent cycles. This rise in impedance is consistent with interfacial void formation, and eventual delamination<sup>22,24</sup>.

This failure mode was not observed in any of the 14 cells tested in which the interfacial Na-K liquid was introduced between the Li metal foil and the solid electrolyte. The example in Supplementary Fig. 9a shows the polarization remaining below 300 mV in the sixth cycle of a cell cycling at areal capacity of  $3.0 \text{ mAh cm}^{-2}$  ( $\sim 15 \mu\text{m}$  Li thickness per half-cycle) at  $1.5 \text{ mA cm}^{-2}$ , which corresponds to a deposited cumulative Li thickness of  $\sim 180 \mu\text{m}$ . We attribute the greater stability at higher per-cycle and cumulative areal capacities to the in situ healing of interfacial defects formed during the Li metal stripping<sup>24</sup>. Kasemchainan et al.<sup>24</sup> found that the effects of void formation can be reduced by the application of a substantial stack pressure (for example, 7 MPa). In our experiments, this failure mode appears to be mitigated even at a very low stack pressure (for example,  $\sim 75 \text{ kPa}$ ; Fig. 5a) on introduction of the interfacial liquid film.

## Conclusions

The CCD at which metal penetration occurs through solid electrolytes and leads to an electrical short circuit was explored for metal electrodes that represent three distinct strategies towards a higher performance: lowering the yield stress of a solid metal electrode, using semi-solid electrodes that consist of co-existing solid and liquid alkali metal phases, and introducing a wetting interfacial liquid film between the electroactive metal and solid electrolyte. With increasing ductility of the pure metal (for example, for Na and K), the CCD is 4–5 times higher than that for pure Li metal. It is possible to further increase the CCD to nearly  $15 \text{ mA cm}^{-2}$  by using a biphasic or semi-solid Na-K electrode. This approach, which yields the high CCD of a liquid metal electrode without sacrificing the packaging advantages of a solid electrode, enables the highest CCD reported to date for any alkali metal electrode at room temperature. When a thin film of interfacial Na-K liquid is introduced between the Li metal and solid electrolyte, a factor of

two increase in the CCD is accompanied by the ability to cycle to areal capacities greater than  $3.5 \text{ mAh cm}^{-2}$  at stack pressures as low as 75 kPa. For both the semi-solid electrode approach and the interfacial liquid-film approach, the ability to cycle at high areal capacities without an impedance rise indicates that failure modes, such as interfacial void formation, can be averted. These design approaches can be extended to other alloy systems. Further development of these strategies may be fruitful in the pursuit of high-energy density all-solid-state batteries.

## Methods

**Materials.** *Solid electrolytes.* Polycrystalline LLZTO was obtained from Toshiba Manufacturing Inc. and NBA and KBA samples were obtained from Ionotec. All the electrolytes had dimensions of 12.7 mm diameter and  $\sim 1$  mm thickness. The crystal structure, single crystallinity and phase purity of the electrolytes were determined via X-ray diffraction using a PANalytical X'Pert Pro diffractometer (Malvern Panalytical Ltd) (Supplementary Table 3).

Electrochemical impedance spectroscopy was performed on the solid electrolytes using sputtered Au electrodes (blocking Li, Na and K ions) on either side of the solid electrolyte disc using a Bio-Logic VMP-3 cell test system. The Au thin film ( $\sim 100$  nm), which acts as the electrical contact between the ceramic electrolyte disc and the test system, was deposited onto the electrolyte via magnetron sputtering (Cressington). Values for ionic conductivity (and dielectric capacitance) were extrapolated from circuit fitting of the resulting impedance spectra (Supplementary Fig. 3).

A Vickers micro-indenter (LECO LM248AT Microindentation Hardness Testing System) was used to place several indents under enough applied load to produce cracks that emanate from the corners. These cracks have a semicircular crack front that extends normal to the surface into the crystal. By varying the applied load, a range of crack lengths is produced. A scanning electron microscopy image of an indent showing the characteristic corner cracks is shown in Supplementary Fig. 2. Indentation loads of 19.6, 9.81 and 4.91 N were used to determine the fracture toughness in this study. The crack lengths were measured via optical microscopy. The corresponding hardness (determined from the square-pyramid indent size) and fracture toughness (determined from the crack length) of the solid electrolytes are summarized in Supplementary Fig. 2.

Two independent methods (Anstis et al.<sup>44</sup> and Evans and Charles<sup>45</sup>) to obtain the fracture toughness from indentation data were used. The Anstis method requires a value for Young's modulus of the indented material<sup>44</sup>, whereas the Evans method is modulus independent<sup>45</sup>. The results are shown in Supplementary Fig. 2.

The ground electrolyte discs (1 mm thickness) received from the vendor were polished using an EcoMe 250 Pro Grinder Polisher (Buehler). To obtain finely polished faces, the samples were then sequentially polished using aqueous diamond suspensions of 9 and 1  $\mu\text{m}$  particle sizes for 25 and 10 min, respectively. The samples were then ultrasonically cleaned in deionized water to remove polishing debris.

Thermal etching of the polished solid electrolytes (1 h at 50, 1,000 and 1,000 °C for LLZTO, NBA and KBA, respectively) revealed the grain size to range from 5 to 10  $\mu\text{m}$  for all three solid electrolytes. Scanning electron microscopy imaging of the samples was conducted using a JEOL 6610 LV SEM (JEOL USA Inc.) operated at a 15 kV accelerating potential and 215 pA current. All the samples were prepared in an argon-filled glove box (oxygen and water levels below 0.1 ppm).

Stylus profilometry was conducted using a Bruker DXT Stylus Profilometer (Bruker) to quantify the roughness of the polished samples. Representative data are shown in Supplementary Fig. 1.

**Alkali metals.** Li foil (750 mm) was sourced from Alfa Aesar. Cubes of Na and K immersed in mineral oil were sourced from Sigma Aldrich. The Li metal was prepared for the cell assembly by cold rolling to the desired thickness between polyethylene sheets and punching a disc of the desired diameter. The Na and K metal electrodes were melted in a glove box and applied as a liquid to the surfaces of the solid electrolyte discs held at room temperature, whereupon the liquid metals quickly froze. The Na–K alloys were prepared by melting the pure Na and K, pipetting by volume into a glass vial in the desired ratio of metals, homogenizing by heating into a single-phase liquid regime and cooling.

**Microhardness testing.** Li metal rods (Millipore Sigma, item 265969), Na metal bars (Alfa Aesar, item L13285), and K metal lumps (Alfa Aesar, item 13267) were sectioned using a razor blade into pieces approximately 25.4 mm diameter by 19.05 mm thick within an argon-filled glove box. The bottom surface of each sample was rigidly fixed to a 12.7 mm stainless-steel plate using cyanoacrylate adhesive. This assembly was then placed between two well-oiled borosilicate glass plates (6.35 mm thick, lubricated with white mineral oil) inside a hydraulic crimper. Subsequently, the pieces were pressed until flat and covered with a thick ( $\sim 3$  mm) layer of petroleum jelly. The resulting samples were removed from the glove box and microhardness tests were conducted through the petroleum jelly using a Phase II+ 900-390A microhardness tester. The loading to maximum force (0.245 N) occurred

over 15 s. Hardness measurements were calculated as the applied load (0.245 N) divided by the projected contact area.

**Electrochemical cell assembly.** Prior to assembly, the polished solid electrolyte discs were heat treated in an argon-filled glove box at oxygen and water contents below 0.1 and 0.1 ppm, respectively, which has been shown to remove surface impurity layers on the electrolyte and reduce the interfacial impedance<sup>45</sup>. Polished LLZTO discs were heat treated in the glove box at 500 °C for 3 h to remove  $\text{LiCO}_3$  and  $\text{LiOH}$  (ref. 45). The NBA and KBA pellets were subjected to heat treatment at 1,000 °C for 1 h in the glove box to remove possible chemisorbed moisture.

Li metal symmetric cells were assembled by placing a disc of flat lithium foil (9.53 mm diameter, 0.25 mm thickness,  $50 \text{ mAh cm}^{-2}$  and  $\sim 20 \mu\text{Li}$ ) between the LLZTO solid electrolyte with a stainless-steel cylinder acting as the current collector on either side. Before the electrochemical cycling, the Li cells were heated to 170 °C for 3 h at an applied stack pressure of 1.5 MPa (calibrated independently with a compression force gauge), which reduced the interfacial impedance of the cell. The area-specific interfacial impedance of the cells was measured to be on the order of  $25\text{--}35 \Omega \text{ cm}^{-2}$ . For cells cycled under even lower pressure ( $\sim 75$  kPa), the springs in the fixture were compressed to a few percent strain based on visual inspection.

Na metal, K metal and Na–K alloy cells were assembled by pipetting a 10  $\mu\text{l}$  drop of molten Na, K or premixed Na–K alloy onto their respective solid electrolytes and flattening the droplet with the steel current collector (7.14 mm diameter) under an applied stack pressure of 1.5 MPa. No precycling heat treatment was necessary to produce a low impedance cell for testing. The capacity of the electrode and its composition change during cycling was computed on the basis of the starting electrode volume and the areal capacity reached during cycling, assuming a linear rule of mixtures for the densities of the Na–K alloys.

Li metal cells that incorporate the eutectic Na–K alloy layer were assembled in a similar manner to those of the plain Li cells by adding  $\sim 5 \mu\text{l}$  of eutectic Na–K alloy (68 mol% K) to one face of the punched Li disc. The side of the Li disc with the added Na–K alloy was placed in contact with the LLZTO solid electrolyte disc. For some of the cells in which a Li metal electrode was used with an interfacial layer of Na–K eutectic liquid, the stack pressure was reduced to a low value of  $\sim 75$  kPa.

**Electrochemical cycling.** Galvanostatic experiments were conducted on the cells at 22 °C using a Bio-Logic VMP-3 cell test system. Li/LLZTO/Li cells were subjected to galvanostatic cycling at nominal current densities (that is, based on the initial electrode areas) from 0.125 to  $1.5 \text{ mA cm}^{-2}$  using 0.125  $\text{mA cm}^{-2}$  increments at nominal areal capacities of  $1.5 \text{ mAh cm}^{-2}$  per cycle (7.5  $\mu\text{m}$  Li plating thickness). Na/NBA/Na, K/KBA/K, 0.95K–0.05Na/KBA/0.95K–0.05Na and 0.90K–0.10Na/KBA/0.90K–0.10Na cells were subjected to galvanostatic cycling at nominal current densities from 0.5 to  $40 \text{ mA cm}^{-2}$  using 0.5  $\text{mA cm}^{-2}$  increments at nominal areal capacities of 3.0  $\text{mAh cm}^{-2}$  per cycle (27.4 and 51.5  $\mu\text{m}$  thickness for Na and K, respectively). NaK(e)-Li/LLZTO/NaK(e)-Li cells were subjected to galvanostatic cycling at nominal current densities from 0.25 to  $3.0 \text{ mA cm}^{-2}$  using 0.25  $\text{mA cm}^{-2}$  increments at nominal areal capacities of 0.25, 1.5 or 3  $\text{mAh cm}^{-2}$  per cycle (1.25, 7.5 or 15  $\mu\text{m}$  Li plating thickness, respectively). This was done to investigate the areal capacity dependence of CCD and to compare present results with literature.

Impedance spectra were collected at the start of testing and at set intervals thereafter (after each galvanostatic cycle for Li/LLZTO/Li and NaK(e)-Li/LLZTO/NaK(e)-Li cells, and after every four cycles for Na/NBA/Na, K/KBA/K, 0.95K–0.05Na/KBA/0.95K–0.05Na and 0.90K–0.10Na/KBA/0.90K–0.10Na cells). Throughout the electrochemical testing, cells remained in an argon-filled glove box with the oxygen and water content below 0.1 and 0.1 ppm, respectively.

We also attempted electrochemical cycling of  $\text{Na}^+$  from Na–K through NBA. However, we observed that NBA disintegrated immediately in the presence of K and Na–K. This finding is consistent with the work of Baclig et al.<sup>40</sup>, who demonstrated that NBA is chemically unstable to K metal.

**Post-mortem characterization.** On completion of the electrochemical cycling, ex situ microscopy was conducted on disassembled cells using a Leica DMS300 (Leica Camera) digital microscope.

**Phase diagrams.** The binary phase diagrams for the Li–Na, Li–K and Na–K systems and the ternary isothermal section of Li–Na–K were calculated using Thermo-Calc software based on the thermodynamic model constructed by the CALPHAD (calculation of phase diagram) modelling approach, in which thermochemical data and phase equilibrium information are used to evaluate the optimal set of parameters that describe the Gibbs energy of each individual phase in a thermodynamic system<sup>46</sup>. The gas phase is described by an ideal substitutional model, with the Gibbs energies of all the constituents taken from the Scientific Group Thermodata Europe database<sup>47</sup>. The molar Gibbs energies of the liquid phase and the three solid-solution phases (face-centred cubic, BCC and hexagonal close packed) that consists of  $n$  components are described by:

$$G_m^{\circ} = \sum_{i=1}^n x_{A_i}^{\circ} G_{A_i}^{\circ} + RT \sum_{i=1}^n x_{A_i}^{\circ} \ln x_{A_i}^{\circ} + \Delta G^{\circ} \quad (1)$$

here  $\varphi$  represents a solution phase that includes elements  $\{A_i | 1 \leq i \leq n, i \in \mathbb{N}\}$ ,  $x_{A_i}^\varphi$  the molar fraction of  $A_i$  in  $\varphi$ ,  $G_{A_i}^\varphi$  the molar Gibbs energy of pure  $A_i$  in the structure of  $\varphi$ ,  $R$  the gas constant,  $T$  the temperature and the excess Gibbs energy, which is expanded as (up to ternary interactions):

$$\Delta G^\varphi = \sum_{i < j} x_{A_i}^\varphi x_{A_j}^\varphi I_{A_i, A_j} + \sum_{i < j < k} x_{A_i}^\varphi x_{A_j}^\varphi x_{A_k}^\varphi I_{A_i, A_j, A_k} \quad (2)$$

where the binary interaction  $I_{A_i, A_j}$  can be expressed in the Redlich–Kister polynomial<sup>48</sup>:

$$I_{A_i, A_j} = \sum_{k=0}^k L_{A_i, A_j}^k \left( x_{A_i}^\varphi - x_{A_j}^\varphi \right)^k \quad (3)$$

where the coefficient  $L_{A_i, A_j}^k = {}^k X_{A_i, A_j} + {}^k Y_{A_i, A_j} T$  describes the non-ideal interaction between  $A_i$  and  $A_j$ , with  ${}^k X_{A_i, A_j}$  and  ${}^k Y_{A_i, A_j}$  as the model parameters. The ternary interaction  $I_{A_i, A_j, A_k}$  can be written as<sup>49</sup>:

$$I_{A_i, A_j, A_k} = \nu_{A_i} A_i L_{A_i, A_j, A_k} + \nu_{A_j} A_j L_{A_i, A_j, A_k} + \nu_{A_k} A_k L_{A_i, A_j, A_k} \quad (4)$$

where  $A_i L_{A_i, A_j, A_k}$ ,  $A_j L_{A_i, A_j, A_k}$  and  $A_k L_{A_i, A_j, A_k}$  are model parameters, and the following definitions are used:

$$\nu_{A_i} = x_{A_i}^\varphi + \frac{1 - x_{A_i}^\varphi - x_{A_j}^\varphi - x_{A_k}^\varphi}{3} \quad (5)$$

$$\nu_{A_j} = x_{A_j}^\varphi + \frac{1 - x_{A_i}^\varphi - x_{A_j}^\varphi - x_{A_k}^\varphi}{3} \quad (6)$$

$$\nu_{A_k} = x_{A_k}^\varphi + \frac{1 - x_{A_i}^\varphi - x_{A_j}^\varphi - x_{A_k}^\varphi}{3} \quad (7)$$

In this work, the Gibbs energies of pure elements are taken from the Scientific Group Thermodata Europe database<sup>50</sup>, and the interaction parameters of the solution phases, as well as the Gibbs energy of the only stable intermetallic compound  $\text{Na}_2\text{K}$ , is adopted from the work of Zhang<sup>51</sup>.

**Microstructural simulation.** The microstructure insets in Fig. 6a were computed with a time-cone method algorithm<sup>51</sup>. All the nuclei were placed at time = 0 with locations obtained from a uniform random distribution, but with a minimum separation between each nucleus. Each nucleus was given a growth speed chosen from a random distribution from 0.6 to 1.5. The areal density of the nuclei and the time slice of the cones determined the final phase fractions, which were established by pixel counting. The time slices for the phase fractions 0.51 and 0.10 were obtained by a secant-search algorithm.

## Data availability

All the relevant data are included in the paper and its Supplementary Information. Source data are provided with this paper.

Received: 29 June 2020; Accepted: 27 January 2021;

Published online: 15 March 2021

## References

- Howell, D., Cunningham, B. Duong, T. & Faguy, P. *Overview of DOE Vehicle Technologies Office Advanced Battery R&D Program* (Vehicle Technologies Office, 2016).
- Harlow, J. E. et al. A wide range of testing results on an excellent lithium-ion cell chemistry to be used as benchmarks for new battery technologies. *J. Electrochem. Soc.* **166**, A3031–A3044 (2019).
- Bills, A., Sripad, S., Fredericks, W. L., Singh, M. & Viswanathan, V. Performance metrics required of next-generation batteries to electrify commercial aircraft. *ACS Energy Lett.* **5**, 663–668 (2020).
- Albertus, P., Babinec, S., Litzelman, S. & Newman, A. Status and challenges in enabling the lithium metal electrode for high-energy and low-cost rechargeable batteries. *Nat. Energy* **3**, 16–21 (2018).
- Aurbach, D., Zinigrad, E., Cohen, Y. & Teller, H. A short review of failure mechanisms of lithium metal and lithiated graphite anodes in liquid electrolyte solutions. *Solid State Ion.* **148**, 405–416 (2002).
- Liu, Z. et al. Interfacial study on solid electrolyte interphase at Li metal anode: implication for Li dendrite growth. *J. Electrochem. Soc.* **163**, A592–A598 (2016).
- Manthiram, A., Yu, X. & Wang, S. Lithium battery chemistries enabled by solid-state electrolytes. *Nat. Rev. Mater.* **2**, 16103 (2017).
- Kerman, K., Luntz, A., Viswanathan, V., Chiang, Y.-M. & Chen, Z. Practical challenges hindering the development of solid state Li ion batteries. *J. Electrochem. Soc.* **164**, A1731–A1744 (2017).
- Janek, J. & Zeier, W. G. A solid future for battery development. *Nat. Energy* **1**, 16141 (2016).
- Thangadurai, V., Narayanan, S. & Pinzaru, D. Garnet-type solid-state fast Li ion conductors for Li batteries: critical review. *Chem. Soc. Rev.* **43**, 4714–4727 (2014).
- Liu, D. et al. Recent progress in sulfide-based solid electrolytes for Li-ion batteries. *Mater. Sci. Eng. B* **213**, 169–176 (2016).
- McGrogan, F. et al. Compliant yet brittle mechanical behavior of  $\text{Li}_2\text{S}-\text{P}_2\text{S}_5$  lithium-ion-conducting solid electrolyte. *Adv. Energy Mater.* **7**, 1602011 (2017).
- Wolfenstine, J. et al. A preliminary investigation of fracture toughness of  $\text{Li}_2\text{La}_3\text{Zr}_2\text{O}_{12}$  and its comparison to other solid Li-ion conductors. *Mater. Lett.* **96**, 117–120 (2013).
- Monroe, C. & Newman, J. The impact of elastic deformation on deposition kinetics at lithium/polymer interfaces. *J. Electrochem. Soc.* **152**, A396–A404 (2005).
- Porz, L. et al. Mechanism of lithium metal penetration through inorganic solid electrolytes. *Adv. Energy Mater.* **7**, 1701003 (2017).
- Swamy, T. et al. Lithium metal penetration induced by electrodeposition through solid electrolytes: example in single-crystal  $\text{Li}_6\text{La}_3\text{ZrTaO}_{12}$  garnet. *J. Electrochem. Soc.* **165**, A3648–A3655 (2018).
- Aguesse, F. et al. Investigating the dendritic growth during full cell cycling of garnet electrolyte in direct contact with Li metal. *ACS Appl. Mater. Interfaces* **9**, 3808–3816 (2017).
- Sharafi, A., Meyer, H. M., Nanda, J., Wolfenstine, J. & Sakamoto, J. Characterizing the Li–Li<sub>2</sub>La<sub>3</sub>Zr<sub>2</sub>O<sub>12</sub> interface stability and kinetics as a function of temperature and current density. *J. Power Sources* **302**, 135–139 (2016).
- Ren, Y. Y., Shen, Y., Lin, Y. H. & Nan, C. W. Direct observation of lithium dendrites inside garnet-type lithium-ion solid electrolyte. *Electrochem. Commun.* **57**, 27–30 (2015).
- Nagao, M. et al. In situ SEM study of a lithium deposition and dissolution mechanism in a bulk-type solid-state cell with a  $\text{Li}_2\text{S}-\text{P}_2\text{S}_5$  solid electrolyte. *Phys. Chem. Chem. Phys.* **15**, 18600–18606 (2013).
- Taylor, N. J. et al. Demonstration of high current densities and extended cycling in the garnet  $\text{Li}_2\text{La}_3\text{Zr}_2\text{O}_{12}$  solid electrolyte. *J. Power Sources* **396**, 314–318 (2018).
- Jolly, D. S. et al. Sodium/Na  $\beta''$  alumina interface: effect of pressure on voids. *ACS Appl. Mater. Interfaces* **12**, 678–685 (2020).
- Bay, M.-C. et al. Sodium plating from Na- $\beta''$ -alumina ceramics at room temperature, paving the way for fast-charging all-solid-state batteries. *Adv. Energy Mater.* **10**, 1902899 (2019).
- Kasemchainan, J. et al. Critical stripping current leads to dendrite formation on plating in lithium anode solid electrolyte cells. *Nat. Mater.* **18**, 1105–1111 (2019).
- Griffith, A. A. The phenomena of rupture and flow in solids. *Phil. Trans. Roy. Soc.* **221A**, 163–198 (1920).
- Inglis, C. E. Stresses in a plate due to the presence of cracks and sharp notches. *Trans. Roy. Inst. Nav. Archit.* **55**, 219–241 (1913).
- Orowan, E. Fracture and strength of solids. *Rep. Prog. Phys.* **12**, 185–232 (1949).
- Virkar, A. V. & Viswanathan, L. Sodium penetration in rapid ion conductors. *J. Am. Ceram. Soc.* **62**, 528–529 (1979).
- Virkar, A. V. On some aspects of breakdown of  $\beta''$ -alumina solid electrolyte. *J. Mater. Sci.* **16**, 1142–1150 (1981).
- Fincher, C. D., Ojeda, D., Zhang, Y., Pharr, G. M. & Pharr, M. Mechanical properties of metallic lithium: from nano to bulk scales. *Acta Mater.* **186**, 215–222 (2019).
- LePage, W. S. et al. Lithium mechanics: roles of strain rate and temperature and implications for lithium metal batteries. *J. Electrochem. Soc.* **166**, A89–A97 (2019).
- Xu, C., Ahmad, Z., Aryanfar, A., Viswanathan, V. & Greer, J. R. Enhanced strength and temperature dependence of mechanical properties of Li at small scales and its implications for Li metal anodes. *Proc. Natl Acad. Sci. USA* **114**, 57–61 (2017).
- Vaks, V. G., Kravchuk, S. P., Zarochentsev, E. V. & Safronov, V. P. Temperature dependence of the elastic constants in alkali metals. *J. Phys. F* **8**, 725–742 (1978).
- Hull, D. & Rosenberg, H. M. The deformation of lithium, sodium and potassium at low temperatures: tensile and resistivity experiments. *Philos. Mag.* **4**, 303–315 (1959).
- Andrade, E. Nd.-C. & Dobbs, E. R. The viscosities of liquid lithium, rubidium and caesium. *Proc. R. Soc. Lond. A* **211**, 12–30 (1952).
- Grosse, A. V. Viscosities of liquid sodium and potassium, from their melting points to their critical points. *Science* **147**, 1438–1441 (1965).
- Fincher, C. D., Zhang, Y., Pharr, G. M. & Pharr, M. Elastic and plastic characteristics of sodium metal. *ACS Appl. Energy Mater.* **3**, 1759–1767 (2020).
- Tabor, D. *The Hardness of Metals* (Oxford Univ. Press, 2000).
- Bates, J. B., Dudney, N. J., Neudecker, B., Ueda, A. & Evans, C. D. Thin-film lithium and lithium-ion batteries. *Solid State Ion.* **135**, 33–45 (2000).
- Bacig, A. C. et al. High-voltage, room-temperature liquid metal flow battery enabled by Na–K[K– $\beta''$ -alumina stability. *Joule* **2**, 1287–1296 (2018).

41. Liu, C., Shamie, J. S., Shaw, L. L. & Sprenkle, V. L. An ambient temperature molten sodium–vanadium battery with aqueous flowing catholyte. *ACS Appl. Mater. Interfaces* **8**, 1545–1552 (2015).
42. Guo, X. et al. A self-healing room-temperature liquid-metal anode for alkali-ion batteries. *Adv. Funct. Mater.* **28**, 1804649 (2018).
43. Sharafi, A. et al. Surface chemistry mechanism of ultra-low interfacial resistance in the solid-state electrolyte  $\text{Li}_x\text{La}_y\text{Zr}_z\text{O}_{12}$ . *Chem. Mater.* **29**, 7961–7968 (2017).
44. Anstis, G. R., Chantikul, P., Lawn, B. R. & Marshall, D. B. A critical evaluation of indentation techniques for measuring fracture toughness: I, direct crack measurements. *J. Am. Ceram. Soc.* **64**, 533–538 (1981).
45. Evans, A. G. & Charles, E. A. Fracture toughness determinations by indentation. *J. Am. Ceram. Soc.* **59**, 371–372 (1976).
46. Kaufman, L. The lattice stability of metals—I. Titanium and zirconium. *Acta Metall.* **7**, 575–587 (1959).
47. Dinsdale, A. T. SGTE data for pure elements. *Calphad* **15**, 317–425 (1991).
48. Redlich, O. & Kister, S. T. Algebraic representation of thermodynamic properties and the classification of solutions. *Ind. Eng. Chem.* **20**, 345–348 (1948).
49. Lukas, H., Fries, S. G. & Sundman, B. *Computational Thermodynamics: the CALPHAD Method* (Cambridge Univ. Press, 2007).
50. Zhang, S. J. *Thermodynamic Investigation of the Effect of Alkali Metal Impurities on the Processing of Al and Mg Alloys* PhD thesis (Pennsylvania State Univ., 2006).
51. Balluffi, R., Allen, S. M. & Carter, W. C. *Kinetics of Materials* (Wiley, 2005).

## Acknowledgements

We acknowledge support from the US Department of Energy, Office of Basic Energy Science, through award no. DE-SC0002633 (J. Vetrano, Program Manager). This work made use of the MRL MRSEC Shared Experimental Facilities at MIT, supported by the National Science Foundation under award no. DMR-1419807. We also acknowledge use of the MIT Nanomechanical Technology Laboratory (A. Schwartzman, Manager). We

thank T. Swamy for helpful discussions, and N. Katorova and P. Morozova for assistance with alkali metal handling procedures. We acknowledge financial support from the MIT-Skoltech Next Generation Program, award no. 2016-1, for the portion of the work related to K metal. C.D.F. acknowledges the support of the National Science Foundation Graduate Research Fellowship under grant no. 1746932. M.P. acknowledges the support of the National Science Foundation under award no. DMR-1944674.

## Author contributions

Y.-M.C. and R.J.-Y.P. designed the study. R.J.-Y.P. prepared, measured and analysed the results from the electrochemical cells. C.M.E. measured the alkali metal wetting angles. C.D.F. measured the alkali metal mechanical properties. A.F.B. performed the image analysis of disassembled cells. P.G. calculated the Li–Na–K ternary phase diagram. All the authors contributed to writing the manuscript.

## Competing interests

Massachusetts Institute of Technology has filed for patents on the subject matter related to this article in which R.J.-Y.P., Y.-M.C., P.G. and V.V. are listed inventors.

## Additional information

**Supplementary information** The online version contains supplementary material available at <https://doi.org/10.1038/s41560-021-00786-w>.

**Correspondence and requests for materials** should be addressed to Y.-M.C.

**Peer review information** *Nature Energy* thanks Qiang Zhang and the other, anonymous, reviewer(s) for their contribution to the peer review of this work.

**Reprints and permissions information** is available at [www.nature.com/reprints](http://www.nature.com/reprints).

**Publisher's note** Springer Nature remains neutral with regard to jurisdictional claims in published maps and institutional affiliations.

© The Author(s), under exclusive licence to Springer Nature Limited 2021, corrected publication 2021